

# **Cryo-EM Structure of the N501Y SARS-CoV-2 Spike Protein in Complex with a Potent Neutralizing Antibody**

Xing Zhu<sup>1#</sup>, Dhiraj Mannar<sup>1#</sup>, Shanti S. Srivastava<sup>1#</sup>, Alison M. Berezuk<sup>1#</sup>, J. -P. Demers<sup>1</sup>, James W Saville<sup>1</sup>, Karoline Leopold<sup>1</sup>, Wei Li<sup>2</sup>, Dimitar S. Dimitrov<sup>2</sup>, Katharine S. Tuttle<sup>1</sup>, Steven Zhou<sup>1</sup>, Sagar Chittori<sup>1</sup>, Sriram Subramaniam<sup>1\*</sup>

<sup>1</sup>Department of Biochemistry and Molecular Biology, University of British Columbia, Vancouver V6T 1Z3, Canada

<sup>2</sup>Center for Antibody Therapeutics, Division of Infectious Diseases, Department of Medicine, University of Pittsburgh Medical School, 3550 Terrace Str, Pittsburgh, PA 15261, USA.

<sup>#</sup>These authors contributed equally

\*Correspondence: [sriram.subramaniam@ubc.ca](mailto:sriram.subramaniam@ubc.ca)

## **ABSTRACT**

**The recently reported “UK variant” of SARS-CoV-2 is thought to be more infectious than previously circulating strains as a result of several changes, including the N501Y mutation. Here, we report cryo-EM structures of SARS-CoV-2 spike protein ectodomains with and without the N501Y mutation, in complex with the V<sub>H</sub> fragment of the potent neutralizing antibody, V<sub>H</sub>-Fc ab8. The mutation results in localized structural perturbations near Y501, but V<sub>H</sub>-Fc ab8 retains the ability to bind and neutralize pseudotyped viruses expressing the N501Y mutant with efficiencies comparable to that of unmutated viruses. Our results show that despite the higher affinity of ACE2 for the N501Y mutant, it can still be neutralized efficiently by an antibody that binds epitopes in the receptor binding domain of the SARS-CoV-2 spike protein.**

The rapid international spread of SARS-CoV-2 is associated with numerous mutations that alter viral fitness. Mutations have been documented in all four structural proteins encoded by the viral genome including the small envelope glycoprotein, membrane glycoprotein, nucleocapsid protein, and the spike protein. The most prominent mutations are in the spike protein, which mediates entry of the virus into cells by engaging with the angiotensin-converting enzyme-2 (ACE2) receptor. Several structures of SARS-CoV-2 spike protein variants in pre- and post-fusion conformations have been reported, including complexes with ACE2 and a variety of antibodies (*1-13*). Mutations that emerge in the receptor binding domain (RBD) of the spike protein are especially of interest given their potential to alter the kinetics and strength of interaction of the virus with target cells. These mutations could also affect the binding of antibodies capable of binding and blocking engagement of the virus with ACE2.

In December 2020, new variants of SARS-CoV-2 carrying several mutations in the spike protein were documented in the UK (SARS-CoV-2 VOC202012/01) and South Africa (501Y.V2) (*14, 15*). Early epidemiological and clinical findings have indicated that these variants show increased transmissibility in the population (*16*). Despite being phylogenetically distinct, a common feature of both UK and South African variants is the mutation of residue 501 in the RBD from Asn to Tyr (N501Y). X-ray crystallography and cryo-EM structural studies have identified N501 as a key residue in the interaction interface between RBD and ACE2. N501 is involved in critical contacts with several ACE2 residues (*5, 6, 10, 13*). Studies carried out in a mouse model before the identification of the new UK variant have suggested that mutations of residue 501 could be linked to increased receptor binding and infectivity (*17, 18*). Understanding the impact of N501Y on antibody neutralization, ACE2 binding, and viral entry is therefore of fundamental interest in the efforts to prevent the spread of COVID-19.

We recently described the potent neutralization of SARS-CoV-2 with V<sub>H</sub>-Fc ab8, an antibody derived from a large human library of antibody sequences (19). To understand the effects of ab8 binding on the N501Y mutant, we expressed and purified spike protein ectodomains with and without the N501Y mutation in Expi293 cells. A cryo-EM structure of the spike protein ectodomain with the N501Y mutation was obtained at an average resolution of ~ 2.8 Å (Figure S1). The structure shows no significant global changes in secondary or quaternary structure as a result of the mutation when compared to the previously published structure of the spike protein ectodomain with an Asn residue at position 501 (referred to as the “unmutated” form; Figure S2).

Cryo-EM structural analysis of the complex formed between V<sub>H</sub> ab8 and the unmutated spike protein ectodomain shows two distinct quaternary states, both at average resolutions of 2.4 Å (Figures 1, S3). One class (Figure 1A) has two RBDs in the “down” position both bound to V<sub>H</sub> ab8, with the third in a predominantly “up” position, but with weaker density for both the RBD and the bound V<sub>H</sub> ab8 fragment, suggesting that this domain is flexible relative to the rest of the ectodomain. In the second class (Figure 1B), one of the RBDs is in the down position, with two in the up position, each bound to V<sub>H</sub> ab8. Global refinement results in lower resolutions for the RBD regions relative to the rest of the spike, but local refinement of just the RBD- V<sub>H</sub> ab8 regions results in structures with local resolutions better than ~ 3 Å in each case (Figure S3). The interface between the RBD and V<sub>H</sub> ab8 is well-defined with key interactions at the interface mediated by residues in the stretch between V483 and S494, along with a few other interactions contributed by non-contiguous RBD residues (Figures 1C, 1D). Residue 501 of the spike protein RBD is at the periphery of the footprint of ab8, with minimal, if any, interactions with the antibody.



The N501Y trimeric spike protein ectodomain shows a single dominant conformation (Figure 2A) with the same distribution as in the first class presented for the complex with unmutated spike ectodomain (Figure 1A). Two V<sub>H</sub> ab8 fragments are bound to RBDs in the down conformation, with weak density for the other RBD, which is flexible and primarily in the up position. The global average resolution of the map is  $\sim 2.8$  Å, with lower local resolution in the RBD regions, but local refinement yields maps of the V<sub>H</sub> ab8-RBD interface at resolutions better than  $\sim 3$  Å (Figure S4). Cryo-EM density maps unambiguously show the location of residue 501 in both unmutated and N501Y mutant spike protein ectodomains (Figures 2B, C). The presence of the mutation does not significantly alter any of the interactions between the RBD and V<sub>H</sub> ab8 or the overall conformation of the loop (Figure S5). However, replacement of the asparagine residue by the bulkier tyrosine side chain results in subtle local rearrangements, noticeably in the orientations of Y505 and Q498 (Figures 2C, 2D).

Comparison of the structures reported here with those reported for the ACE2-RBD complex from earlier X-ray crystallography and cryo-EM studies enable visualization of the similarities and differences in the modes of binding (Figure 3). ACE2 binding has been observed only to RBDs in the up position, likely because of steric constraints in accommodating ACE2 in the down conformation. In contrast, the much smaller V<sub>H</sub> ab8 fragment binds the RBD both in up and down positions. Despite these differences, and the fact that ACE2 and V<sub>H</sub> ab8 each have distinctive directions of approach in their contact with the RBD, there is a good match in the RBD footprint between V<sub>H</sub> ab8 and ACE2, accounting for the potent neutralization by the V<sub>H</sub>-Fc antibody (19). Residue 501 is located towards the outer edge of the contact zone between RBD in the ACE2 complex and just outside the zone of contact of V<sub>H</sub> ab8 with RBD, providing a

structural rationale for the findings we describe here on the minimal effect of the N501Y mutation on interaction with the antibody.

We next carried out a series of experiments to test the effects of the N501Y mutation on ACE2 binding and the relative strengths of binding and neutralization potency of V<sub>H</sub>-Fc ab8 (Figure 4). HEK293-T cells stably overexpressing ACE2 were incubated with pseudotyped viruses engineered to harbor a luciferase reporter gene expressing spike proteins with or without the N501Y mutation. Luciferase activities in cellular lysates were determined 48-hour post-infection. When normalized to p24 levels in the viruses, the relative luminescence units (RLU) intensity from cells infected by the N501Y mutant was higher than control viruses expressing the unmutated form (N501Y: 6499 +/- 1824 RLU [standard deviation], Unmutated: 3045 +/- 817 RLU [standard deviation]), demonstrating that the N501Y mutation results in increased infectivity. To verify that this was a result of the increased binding strength of the mutant RBD to ACE2, we measured neutralization efficiency as a function of exogenously added soluble ACE2-mFc proteins. The neutralization profiles (Figure 4A) show that IC<sub>50</sub> for neutralization of the mutant is lower, consistent with the hypothesis that the greater infectivity of the N501Y mutant stems from improved binding to ACE2.

Competition experiments establish that ACE2 can displace V<sub>H</sub>-Fc ab8 bound to unmutated and N501Y mutant spike proteins with similar efficiency (Figure 4B). Consistent with these measurements, neutralization experiments carried out with V<sub>H</sub>-Fc ab8 shows that it is able to neutralize the N501Y mutant with a potency similar to that of the unmutated form (Figure 4C). The neutralization studies were further confirmed by ELISA measurements of relative binding efficiency V<sub>H</sub>-Fc ab8. As shown in Figure 4D, the N501Y mutation has no significant effect on

V<sub>H</sub>-Fc ab8 binding. Finally, negative stain studies of the complex formed between trimeric spike proteins and soluble ACE2 show that the N501Y mutant has a higher stoichiometry of ACE2 binding in the presence of similar concentrations of ACE2 (Figures 4E, F). Collectively, the binding, neutralization, and electron microscopic analyses show that the N501Y mutation results in increased efficiency of ACE2 binding, but has relatively minor effects on binding and potency of an antibody that targets neutralizing epitopes in the RBD.

Our studies with the N501Y mutant confirm the expectation that the rapid spread of the UK variant of SARS-CoV-2 is likely due to the viruses being more infectious. While there can be multiple origins for the increased infectivity, our biochemical and structural studies establish that the N501Y mutation results in increased ACE2 binding efficiency. The competition assays with a strongly neutralizing antibody show that it competes for binding with the spike trimer-ACE2 interaction in a concentration-dependent manner. Our results suggest that despite the higher infectivity of SARS-CoV-2 viruses carrying the N501Y mutation, the availability of the extended epitope surface on the RBD will likely enable effective neutralization by antibodies elicited by immunization with vaccines that are currently in production. With the continued spread of SARS-CoV-2, it appears likely that further mutations that enhance viral fitness will emerge. Cryo-EM methods to rapidly identify footprints of antibodies that are generated by current and future generations of vaccines could thus add a critical tool to the arsenal of efforts to prevent and treat COVID-19.

## **Acknowledgments and Funding**

This work was supported by awards to S.S. from a Canada Excellence Research Chair Award, the VGH Foundation and Genome BC, Canada. W.L. and D.S.D. were supported by the University of Pittsburgh Medical Center. D.M. is supported by a CIHR Frederick Banting and Charles Best Canada Graduate Scholarship Master's Award (CGS-M). J.-P.D. is supported by a Long-Term Fellowship from the Human Frontier Science Program. J.W.S is supported by a CIHR Frederick Banting and Charles Best Canada Graduate Scholarships Doctoral Award (CGS D) and a UBC President's Academic Excellence Initiative PhD Award.

**Author contributions.** This work was the result of a concerted team effort from all individuals listed as authors. D.M., K.L., S.S.S., S.Z. and J.W.S. collectively carried out all biochemical aspects including expression, production and purification of the spike proteins and antibody fragments. D.M. carried out the neutralization experiments. A.B., S.C., K.S.T. and J.-P.D. collectively carried out the experimental components of cryo-EM and electron microscopy including specimen preparation and data collection. X.Z. carried out all computational aspects of image processing and structure determination. X.Z., S.S.S. and S.S. interpreted and analyzed the cryo-EM structures. W.L. and D.S.D. provided the plasmids for VH-ab8 as part of a collaboration between the Subramaniam and Dimitrov laboratories on SARS-CoV-2. S.S. led and oversaw research on all aspects of the project and drafted the manuscript with input from all co-authors.

**Competing interests.** All UBC authors declare no competing interests. Wei Li and Dimiter S. Dimitrov are coinventors of a patent, filed by the University of Pittsburgh, related to ab8.

**Data and Materials Availability.** The density maps and atomic coordinates for the structures reported will be made publicly available in the Electron Microscopy Data Bank.

### Figure Legends:

**Figure 1.** Structure of V<sub>H</sub> ab8 bound to spike protein trimer. (A, B) Atomic models for the structures of the two main classes of the complex of V<sub>H</sub> ab8 with the unmutated spike protein ectodomain. Each chain in the spike protein trimer is colored differently, and V<sub>H</sub> ab8 is shown in red. The structure in (A) has two RBDs in the down position with well-resolved densities for the bound V<sub>H</sub> ab8, with the third RBD in the up position, and poorly resolved V<sub>H</sub> ab8 density. The structure in (B) has one RBD in the down position and two RBDs in the up position with well-resolved densities for all three bound V<sub>H</sub> ab8. (C, D) Zoomed-in views of the interface between the RBD in the down position with V<sub>H</sub> ab8 with residues involved in the contact zone labeled. The location of N501 near the edge of the antibody footprint is indicated with a black arrow.

**Figure 2.** Structure of V<sub>H</sub> ab8 bound to spike protein trimer N501Y mutant. (A) Atomic model for the structures of the complex of V<sub>H</sub> ab8 with the N501Y mutant spike protein ectodomain. The structure has two RBDs in the down position with well-resolved densities for the bound V<sub>H</sub> ab8, with the third RBD in the up position, and poorly resolved V<sub>H</sub> ab8 density. (B, C) Views of the density map in the region near 501 for the N501Y mutant spike protein ectodomain (B) and the unmutated form (C).

**Figure 3.** Comparison of footprints of V<sub>H</sub> ab8 and ACE2 on the RBD. (A) Structure of the complex between the ACE2-ectodomain and the RBD of the unmutated spike protein ectodomain (PDB 6LZG). (B) Superposition of the structures of the complex of the RBD with V<sub>H</sub>-Fc and with ACE2 to show the relative footprints of V<sub>H</sub>-Fc and ACE2 on the RBD surface. (C, D) View into the RBD binding interface highlighting the residues that make contact with ACE2 (C) and V<sub>H</sub>-ab8 (D).

**Figure 4.** Analysis of ACE2 and V<sub>H</sub>-FC ab8 interactions with N501Y and unmutated spike. (A) Analysis of N501Y or unmutated SARS-CoV-2 S pseudo-typed virus neutralization by soluble ACE2-mFC. (B) ELISA analysis of N501Y or unmutated SARS-CoV-2 spike ectodomain binding by ACE2 in the presence of serial dilutions of V<sub>H</sub>-FC ab8. (C) N501Y or unmutated SARS-CoV-2 S pseudo-typed virus neutralization by V<sub>H</sub>-FC ab8. (D) ELISA analysis of antibody interactions with either N501Y or unmutated spike ectodomain. (E,F) 3D reconstructions of ACE2 ectodomain – spike complexes for either unmutated spike (E) or spike harboring the N501Y mutation (F). Experiments were done at least in duplicate and the average values are shown. Error bars denote 1 standard deviation about the mean.

**Figure S1.** Cryo-EM data processing and validation for the N501Y spike protein ectodomain. (A) Representative micrograph. (B) 2D class averages. (C) Gold-standard Fourier shell correlation (FSC) plot. (D) Local resolution estimation. (E) Viewing direction distribution.

**Figure S2.** Superposition of the structure of the N501Y spike protein ectodomain (light orange) with the previously published structure of the unmutated construct (blue; PDB ID 6XKL).

**Figure S3.** Cryo-EM data processing and validation for the complex between V<sub>H</sub> ab8 and the spike protein ectodomain. (A) Representative micrograph. (B) 2D class averages. (C-N), Gold-standard Fourier shell correlation (FSC) plot, local resolution estimation and viewing direction distribution, FSC plots for local refinements of class 1 (C-H), in which 2 RBDs are in the down position and 1 RBD is in the up position, and class 2 (I-N), in which 1 RBD is in down position and 2 RBD are in the up position.

**Figure S4.** Cryo-EM data processing and validation for the complex between the N501Y spike protein ectodomain and V<sub>H</sub> Ab8. (A) Representative micrograph. (B) 2D class averages. (C) Gold-standard Fourier shell correlation (FSC) plot. (D) Local resolution estimation. (E) viewing direction distribution. (F-G) FSC plots for local refinement.

**Figure S5.** Superposition of the structures of V<sub>H</sub> ab8 bound to unmutated and N501Y mutant forms of the spike protein ectodomain.

## Materials and Methods

### Cloning, Expression and Purification of Recombinant Spike Protein Constructs

The wild type SARS-CoV-2 S HexaPro expression plasmid was a gift from Jason McLellan (7) and obtained from Addgene (plasmid #154754; <http://n2t.net/addgene:154754>; RRID:Addgene\_154754). The N501Y mutation was introduced by site-directed mutagenesis (Q5 Site-Directed Mutagenesis Kit, New England Biolabs). Successful subcloning and mutation were confirmed by Sanger sequencing (Genewiz, Inc.). Expi293F cells (ThermoFisher) were grown in suspension culture using Expi293 Expression Medium (ThermoFisher) at 37°C, 8% CO<sub>2</sub>. Cells were transiently transfected at a density of 3 x 10<sup>6</sup> cells/mL using linear polyethylenimine (Polysciences). 24 hours following transfection, media was supplemented with 2.2 mM valproic acid and expression carried out for 5 days at 37°C, 8% CO<sub>2</sub>. The supernatant was harvested by centrifugation and filtered through a 0.22 µm filter before loading it onto a 5 mL HisTrap excel column (Cytiva). The column was washed with 20 column volumes of wash buffer (20 mM Tris pH 8.0, 500 mM NaCl), followed by 5 CVs of wash buffer supplemented with 20 mM imidazole. The protein was eluted with elution buffer (20 mM Tris pH 8.0, 500 mM NaCl, 500 mM imidazole). Elution fractions containing the protein were pooled and concentrated (Amicon Ultra 100 kDa cut off, Millipore Sigma) for gel filtration. Gel filtration was conducted using a Superose 6 10/300 GL column (Cytiva) pre-equilibrated with GF buffer (20 mM Tris pH 8.0, 150 mM NaCl). Peak fractions corresponding to soluble protein were pooled and concentrated to 4.5 - 5.5 mg/mL (Amicon Ultra 100 kDa cut off, Millipore Sigma). Protein purity was estimated as > 95% by SDS-PAGE and protein concentration was measured spectrophotometrically (Implen Nanophotometer N60, Implen).



### Negative Stain Sample Preparation and Data Collection

For negative stain, purified S protein (0.05 mg/ml) was mixed with V<sub>H</sub> ab8 (0.02 mg/mL), or soluble ACE2 (0.05 mg/mL) and incubated on ice for 15 mins. For the competition experiment, the S protein (0.05 mg/ml) was first incubated on ice with V<sub>H</sub> ab8 at concentrations of 0.02, 0.05, 1.00 mg/ml for 30 mins, followed by addition of ACE2 (0.05 mg/mL) for another 30 mins. Grids (Cu 200- or 300-mesh coated with continuous ultrathin carbon) were plasma cleaned using an H<sub>2</sub>/O<sub>2</sub> gas mixture for 15 s in a Solarus plasma cleaner (Gatan Inc.) or 10 s in a PELCO easiGlow glow discharge cleaning system (Ted Pella Inc.). The protein mixtures (4.8 µl) were applied to the grid and allowed to adsorb for 30 s before blotting away excess liquid, followed by a brief wash with MilliQ H<sub>2</sub>O. Grids were stained by three successive applications of 2% (w/v) uranyl formate (20 s, 20 s, 60 s). Negative stain grids were imaged using a 200 kV Glacios transmission electron microscope (ThermoFisher Scientific) equipped with a Falcon3 camera operated in linear mode. Micrographs were collected using EPU at nominal 92,000x magnification (physical pixel size 1.6 Å) over a defocus range of -1.0 µm to -2.0 µm with a total accumulated dose of 40 e<sup>-</sup>/Å<sup>2</sup>.

### Cryo-EM Sample Preparation and Data Collection

For cryo-EM, grids were plasma cleaned using an H<sub>2</sub>/O<sub>2</sub> gas mixture for 15 seconds in a Solarus II Plasma Cleaner (Gatan Inc.), before 1.8 µL of protein suspension was applied to the surface of the grid. Using a Vitrobot Mark IV (Thermo Fisher Scientific), the sample was applied to either Quantifoil Holey Carbon R1.2/1.3 300 mesh grids or UltrAuFoil Holey Gold 300 mesh grids at a temperature of 10 °C and a humidity level of 100% and then vitrified in liquid ethane after blotting for 12 seconds with a blot force of -10. All cryo-EM grids were screened using a 200 kV Glacios transmission electron microscope (ThermoFisher Scientific) equipped with a Falcon4

direct electron detector followed by high-resolution data collection on a 300 kV Titan Krios G4 transmission electron microscope (ThermoFisher Scientific) equipped with a Falcon4 direct electron detector in electron event registration (EER) mode. Movies were collected at 155,000x magnification (physical pixel size 0.5 Å) over a defocus range of -1 μm to -3 μm with a total dose of 40 e<sup>-</sup>/Å<sup>2</sup> using EPU automated acquisition software (ThermoFisher).

### Image Processing

In general, all data processing was performed in cryoSPARC v.2.15 or v.3.0.1 (20) unless stated otherwise. For negative stain data, motion correction and CTF estimation were performed in RELION v.3.1.1 (21). Particles were picked by crYOLO v.1.7.6 (22) with a pre-trained model. After extraction, particles were imported into cryoSPARC and subjected to 2D classification and 3D heterogeneous classification. Final density maps were obtained by 3D homogeneous refinement. For cryo-EM data, motion correction in patch mode, CTF estimation in patch mode, reference-free particle picking and particle extraction were performed on-the-fly in cryoSPARC. After preprocessing, particles were subjected to 2D classification and 3D heterogeneous classification. The consensus maps were obtained by 3D homogeneous refinement with per particle CTF estimation and aberration correction. Local refinements with the mask covering single RBD and its bound V<sub>H</sub> ab8 resulted in improvement of the RBD-Ab8 interface. Overall resolution and locally refined resolutions were according to the gold-standard FSC (23).

### Model Building and Refinement

Coordinates of PDB 7CH5\_H were used as initial models to build the V<sub>H</sub> ab8 structure. Individual domains of SARS-CoV-2 HexaPro S trimer (PDB code 6XKL) were docked into cryo-EM density using UCSF Chimera v.1.15 (24). Initial models were first refined against

sharpened locally refined maps, followed by iterative rounds of refinement against consensus map in COOT v.0.9.3 (25) and Phenix v.1.7.1 (26). Glycans were added at N-linked glycosylation sites in COOT. Model validation was performed using MolProbity (27). Figures were prepared using UCSF Chimera, UCSF ChimeraX v.1.1.1 (28), and PyMOL (v.2.2 Schrodinger, LLC).

### Pseudovirus Neutralization Assay

SARS-CoV-2 S N501Y plasmid was obtained from SARS-CoV-2 S plasmid (HDM-IDTSpike-fixK) by site-directed mutagenesis (Q5 Site-Directed Mutagenesis Kit, New England Biolabs). SARS-CoV-2 S and SARS\_CoV-2 S N501Y pseudotyped retroviral particles were produced in HEK293T cells as described previously (29). Briefly, a 3rd generation lentiviral packaging system was utilized in combination with plasmids encoding the full-length SARS-CoV-2 spike, along with a transfer plasmid encoding luciferase and GFP as a dual reporter gene.

Pseudoviruses were harvested 60 hrs after transfection, filtered with 0.45  $\mu$ m PES filters, and frozen. For cell-entry and neutralization assays, HEK293T-ACE2 cells were seeded in 96 well plates at 50,000 cells per well. The next day, pseudoviral preparations normalized for p24 levels (Lenti-X™ GoStix™ Plus) were incubated with dilutions of the indicated antibodies, ACE2-mFc (SinoBiological), or media alone for 1 hr at 37°C prior to addition to cells and incubation for 48 hrs. Cells were then lysed and luciferase activity assessed using the ONE-Glo™ EX Luciferase Assay System (Promega) according to the manufacturer's specifications. Detection of relative luciferase units was carried out using a Varioskan Lux plate reader (ThermoFisher). Percent neutralization was calculated relative to signals obtained in the presence of virus alone for each experiment.

### Enzyme-Linked Immunosorbent Assay (ELISA)

100  $\mu$ l of wild type or N501Y SARS-CoV-2 S protein preparations were coated onto 96-well MaxiSorp™ plates at 2  $\mu$ g/ml in PBS overnight at 4°C. All washing steps were performed 5 times with PBS + 0.05% Tween 20 (PBS-T). After washing, wells were incubated with blocking buffer (PBS-T + 2% BSA) for 1 hr at room temperature. After washing, wells were incubated with dilutions of V<sub>H</sub>-FC ab8 or ACE2-mFC (SinoBiological) in PBS-T + 0.5% BSA buffer for 1 hr at room temperature. After washing, wells were incubated with either goat anti-human IgG (Jackson ImmunoResearch) or goat anti-Mouse IgG Fc Secondary Antibody, HRP (Invitrogen) at a 1:8,000 dilution in PBS-T + 0.5% BSA buffer for 1 hr at room temperature. After washing, the substrate solution (Pierce™ 1-Step™) was used for color development according to the manufacturer's specifications. Optical density at 450 nm was read on a Varioskan Lux plate reader (Thermo Fisher Scientific). For ACE-2 competition assays, experiments were conducted as described above with amendments. Serial dilutions of V<sub>H</sub>-FC ab8 were incubated for 30 mins at room temperature prior to the addition of 2.5 nM ACE2-mFC (SinoBiological). Wells were then further incubated for 45 minutes at room temperature. After washing, wells were incubated at a 1:8,000 dilution of Goat anti-Mouse IgG Fc Secondary Antibody, HRP (Invitrogen) in PBS-T + 0.5% BSA buffer for 1 hr at room temperature. After washing, the substrate solution (Pierce™ 1-Step™) was used for colour development according to the manufacturer's specifications. Optical density at 450 nm was read on a Varioskan Lux plate reader (Thermo Fisher Scientific). For all experiments, controls for antibody- BSA interactions were performed. For competition assays, controls for anti-Mouse IgG Fc Secondary Antibody recognition of V<sub>H</sub>-FC ab8 were performed.

## REFERENCES

1. Y. Cai *et al.*, Distinct conformational states of SARS-CoV-2 spike protein. *Science* **369**, 1586-1592 (2020).
2. R. Henderson *et al.*, Controlling the SARS-CoV-2 spike glycoprotein conformation. *Nat Struct Mol Biol* **27**, 925-933 (2020).
3. D. Wrapp *et al.*, Cryo-EM structure of the 2019-nCoV spike in the prefusion conformation. *Science* **367**, 1260-1263 (2020).
4. A. C. Walls *et al.*, Structure, Function, and Antigenicity of the SARS-CoV-2 Spike Glycoprotein. *Cell* **181**, 281-292 e286 (2020).
5. J. Lan *et al.*, Structure of the SARS-CoV-2 spike receptor-binding domain bound to the ACE2 receptor. *Nature* **581**, 215-220 (2020).
6. D. J. Benton *et al.*, Receptor binding and priming of the spike protein of SARS-CoV-2 for membrane fusion. *Nature* **588**, 327-330 (2020).
7. C. L. Hsieh *et al.*, Structure-based design of prefusion-stabilized SARS-CoV-2 spikes. *Science* **369**, 1501-1505 (2020).
8. Z. Ke *et al.*, Structures and distributions of SARS-CoV-2 spike proteins on intact virions. *Nature* **588**, 498-502 (2020).
9. M. McCallum, A. C. Walls, J. E. Bowen, D. Corti, D. Veisler, Structure-guided covalent stabilization of coronavirus spike glycoprotein trimers in the closed conformation. *Nat Struct Mol Biol* **27**, 942-949 (2020).
10. J. Shang *et al.*, Structural basis of receptor recognition by SARS-CoV-2. *Nature* **581**, 221-224 (2020).
11. H. Yao *et al.*, Molecular Architecture of the SARS-CoV-2 Virus. *Cell* **183**, 730-738 e713 (2020).
12. T. Zhou *et al.*, Cryo-EM Structures of SARS-CoV-2 Spike without and with ACE2 Reveal a pH-Dependent Switch to Mediate Endosomal Positioning of Receptor-Binding Domains. *Cell Host Microbe* **28**, 867-879 e865 (2020).
13. R. Yan *et al.*, Structural basis for the recognition of SARS-CoV-2 by full-length human ACE2. *Science* **367**, 1444-1448 (2020).
14. WHO. (2020), vol. 2021.
15. A. S. Luring, E. B. Hodcroft, Genetic Variants of SARS-CoV-2—What Do They Mean? *JAMA*, (2021).
16. N. G. Davies *et al.*, Estimated transmissibility and severity of novel SARS-CoV-2 Variant of Concern 202012/01 in England. *medRxiv*, 2020.2012.2024.20248822 (2020).
17. H. Gu *et al.*, Adaptation of SARS-CoV-2 in BALB/c mice for testing vaccine efficacy. *Science* **369**, 1603-1607 (2020).
18. T. N. Starr *et al.*, Deep Mutational Scanning of SARS-CoV-2 Receptor Binding Domain Reveals Constraints on Folding and ACE2 Binding. *Cell* **182**, 1295-1310 e1220 (2020).
19. W. Li *et al.*, High Potency of a Bivalent Human VH Domain in SARS-CoV-2 Animal Models. *Cell* **183**, 429-441 e416 (2020).
20. A. Punjani, J. L. Rubinstein, D. J. Fleet, M. A. Brubaker, cryoSPARC: algorithms for rapid unsupervised cryo-EM structure determination. *Nat Methods* **14**, 290-296 (2017).
21. S. H. Scheres, RELION: implementation of a Bayesian approach to cryo-EM structure determination. *J Struct Biol* **180**, 519-530 (2012).
22. T. Wagner *et al.*, SPHIRE-crYOLO is a fast and accurate fully automated particle picker for cryo-EM. *Commun Biol* **2**, 218 (2019).

23. J. M. Bell, M. Chen, P. R. Baldwin, S. J. Ludtke, High resolution single particle refinement in EMAN2.1. *Methods* **100**, 25-34 (2016).
24. E. F. Pettersen *et al.*, UCSF Chimera--a visualization system for exploratory research and analysis. *J Comput Chem* **25**, 1605-1612 (2004).
25. P. Emsley, B. Lohkamp, W. G. Scott, K. Cowtan, Features and development of Coot. *Acta Crystallogr D Biol Crystallogr* **66**, 486-501 (2010).
26. P. D. Adams *et al.*, PHENIX: a comprehensive Python-based system for macromolecular structure solution. *Acta Crystallogr D Biol Crystallogr* **66**, 213-221 (2010).
27. V. B. Chen *et al.*, MolProbity: all-atom structure validation for macromolecular crystallography. *Acta Crystallogr D Biol Crystallogr* **66**, 12-21 (2010).
28. T. D. Goddard *et al.*, UCSF ChimeraX: Meeting modern challenges in visualization and analysis. *Protein Sci* **27**, 14-25 (2018).
29. K. H. D. Crawford *et al.*, Protocol and Reagents for Pseudotyping Lentiviral Particles with SARS-CoV-2 Spike Protein for Neutralization Assays. *Viruses* **12**, (2020).



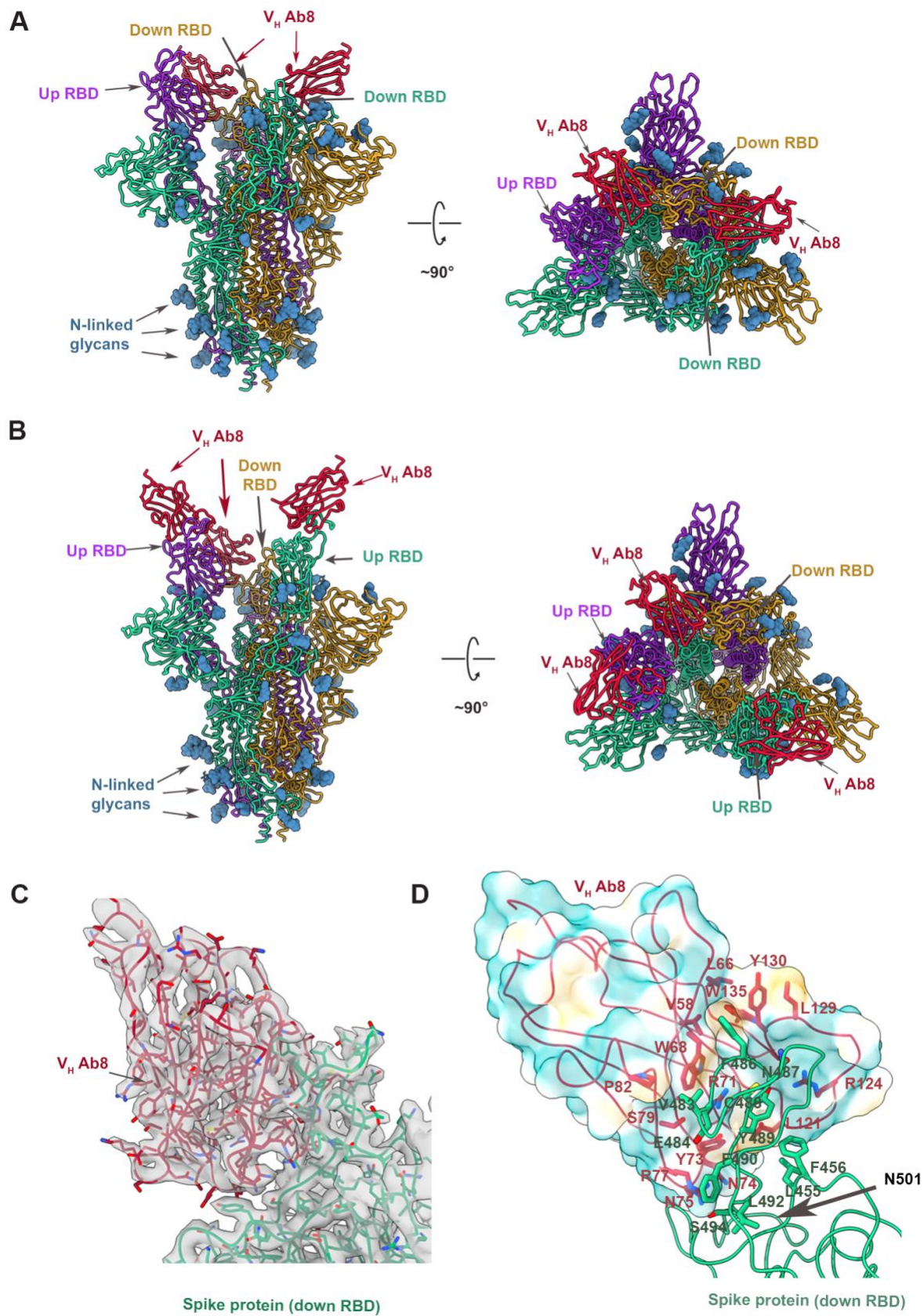
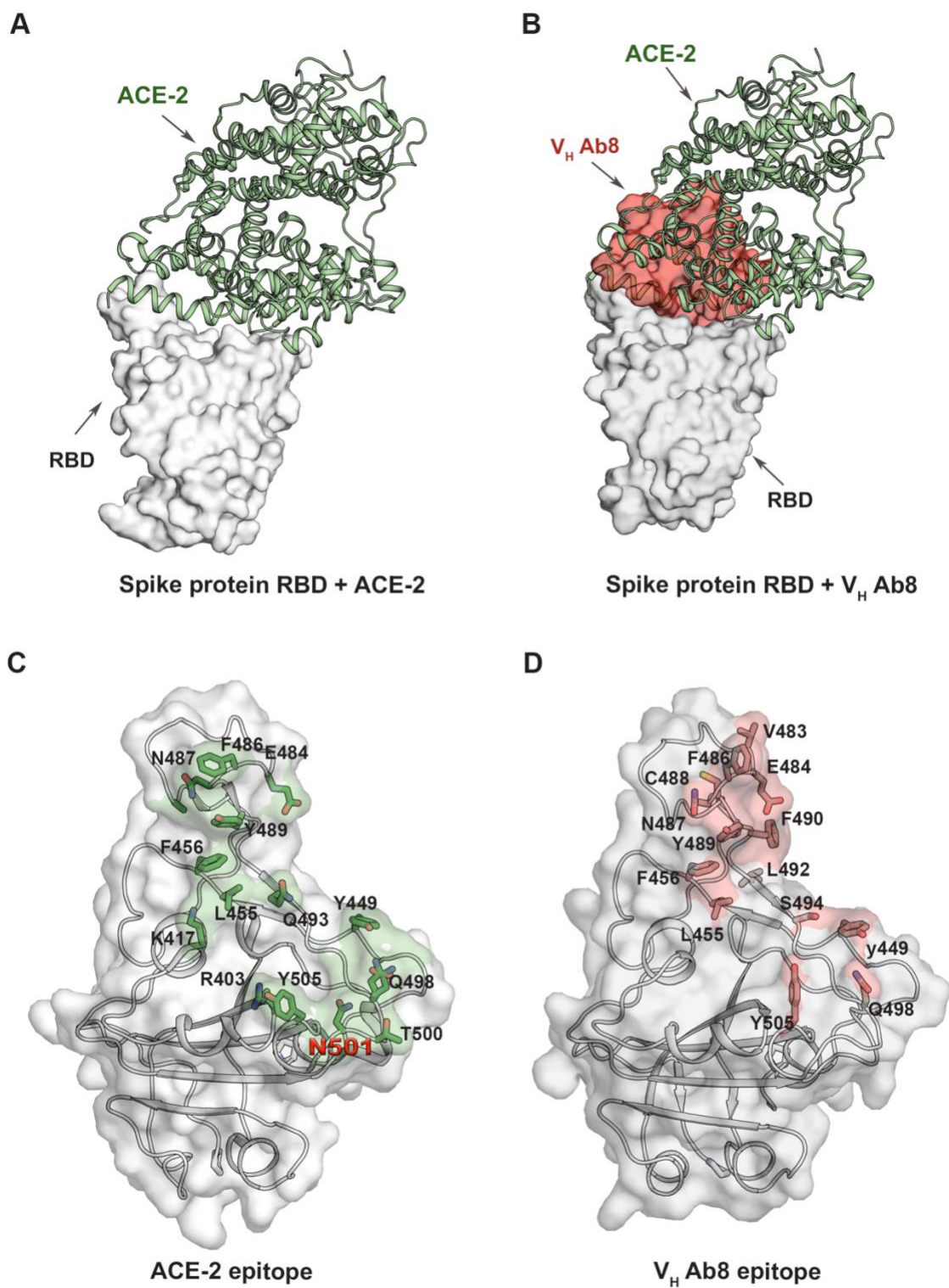


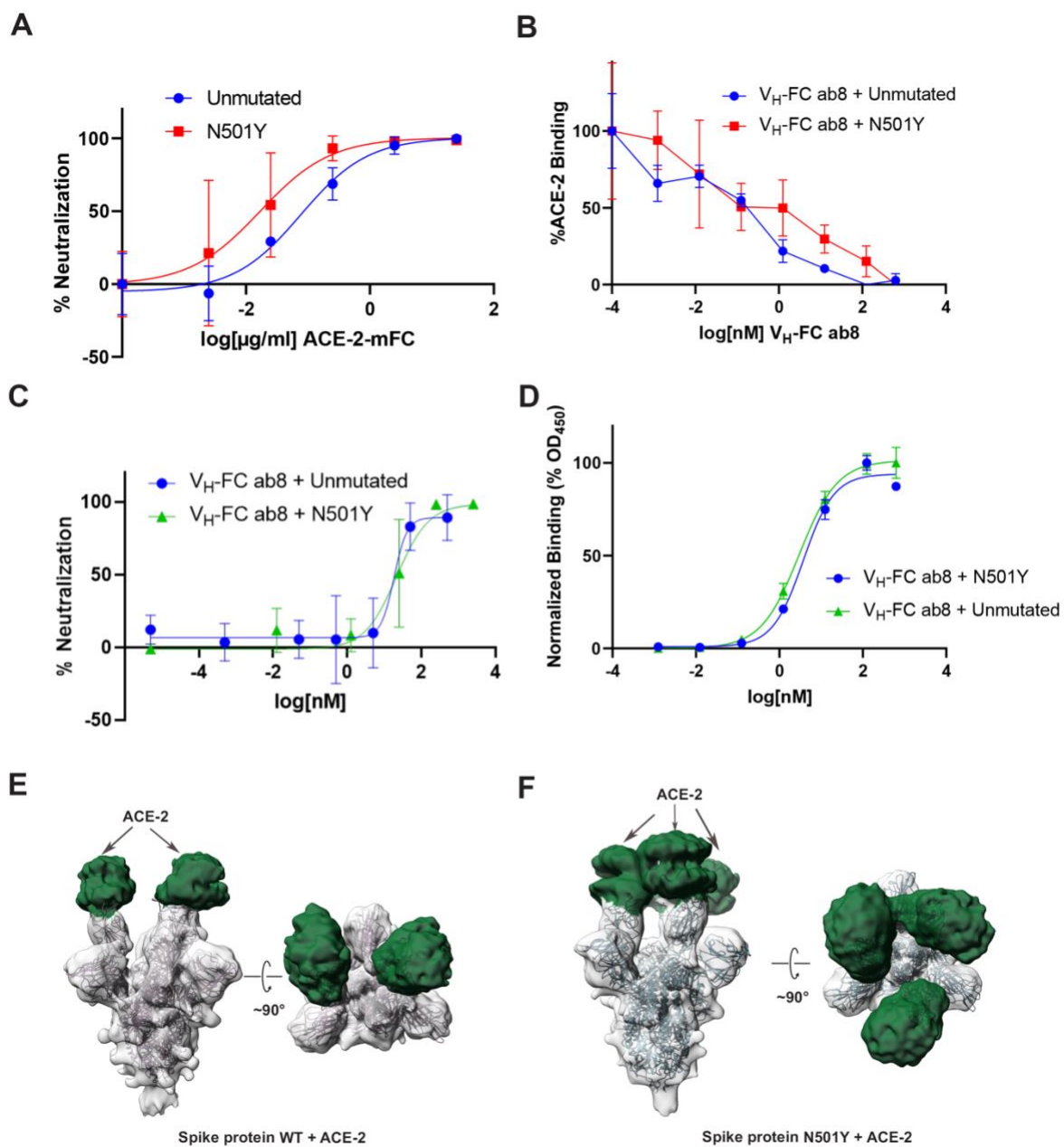
Figure 1







**Figure 3**



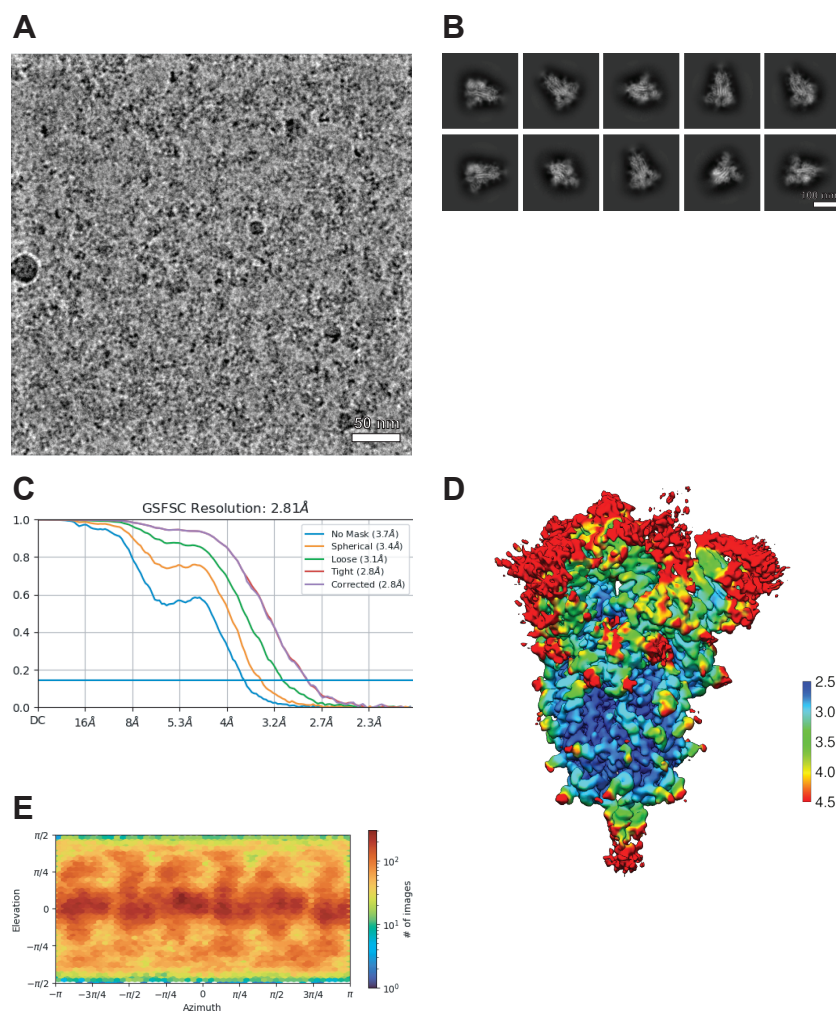
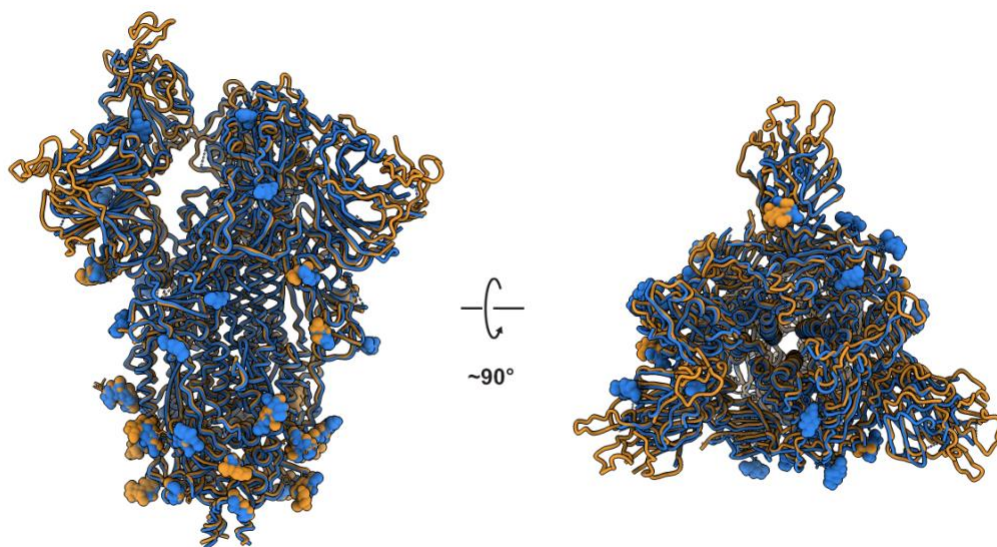


Figure S1



**Figure S2**



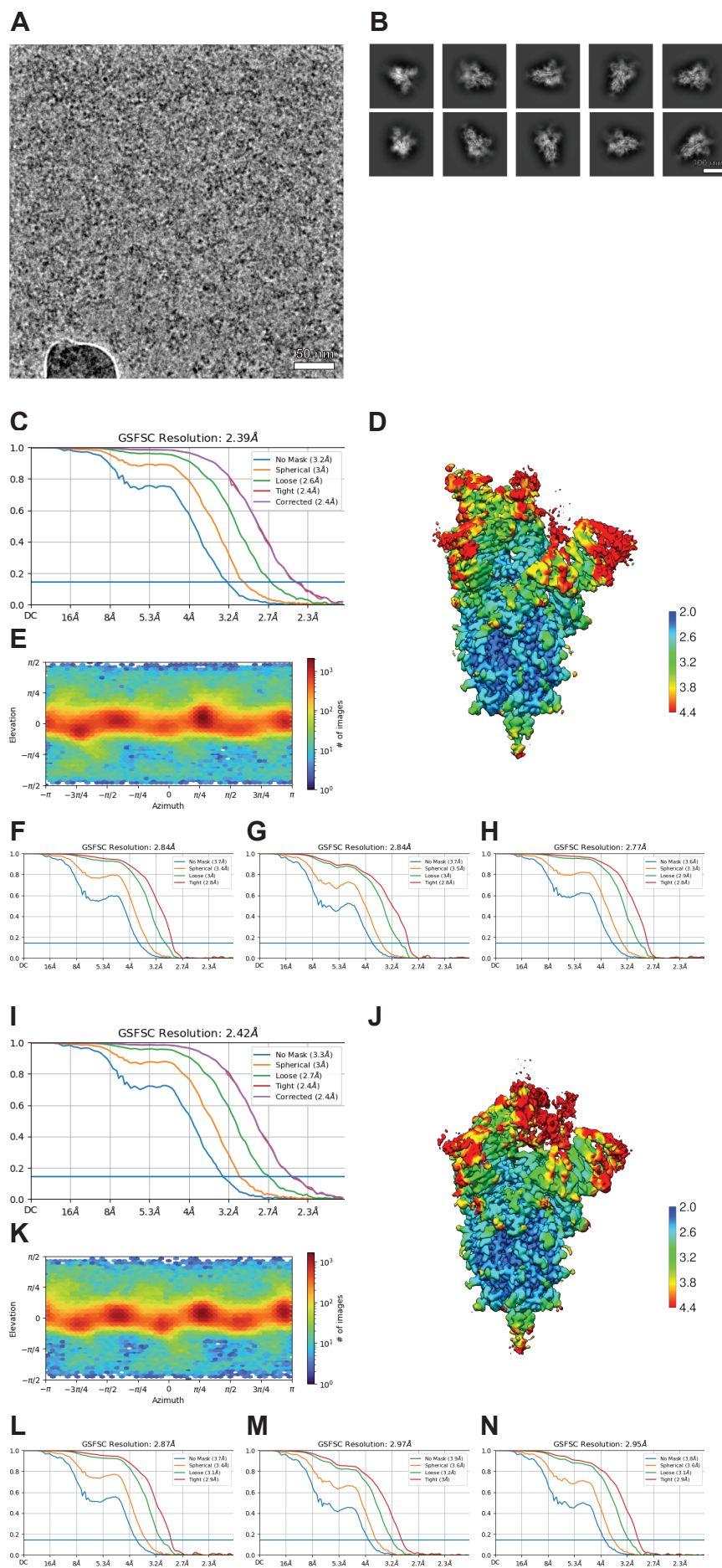


Figure S3

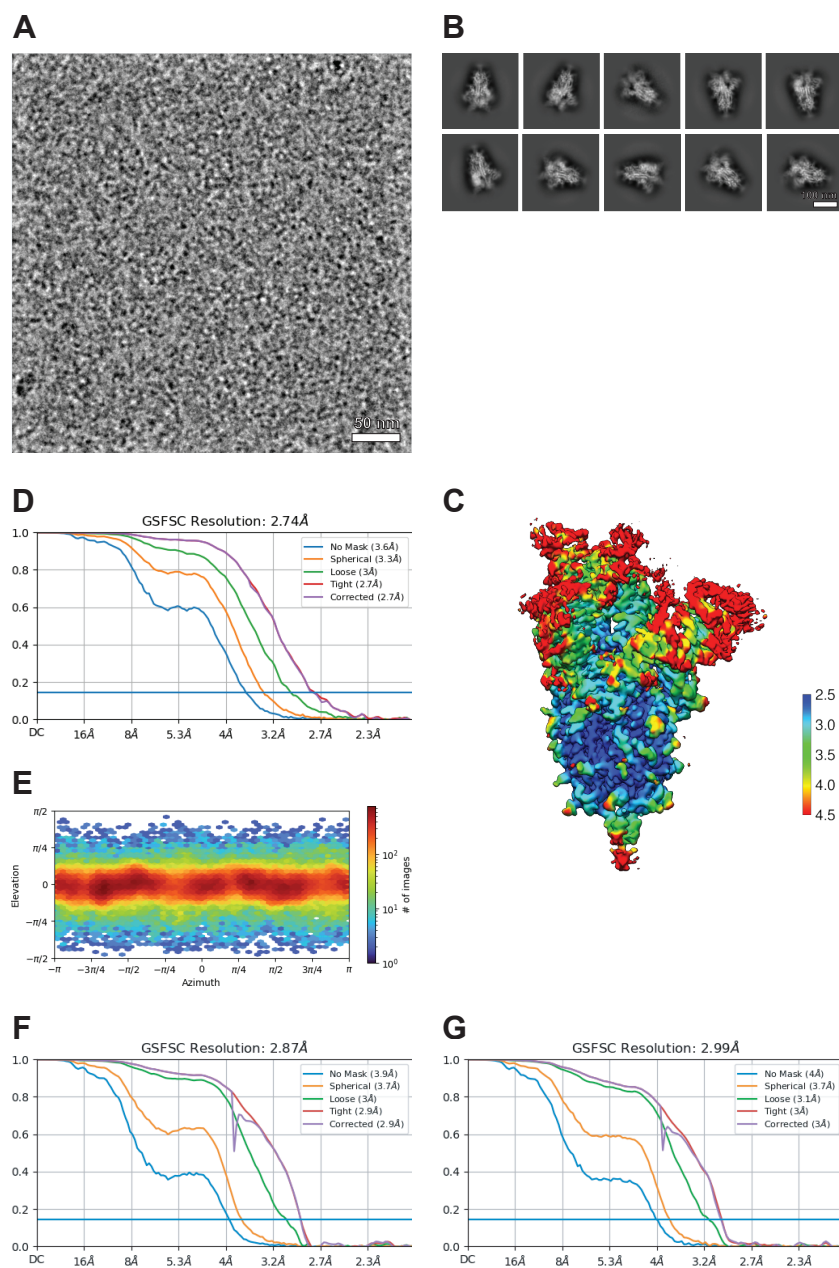


Figure S4

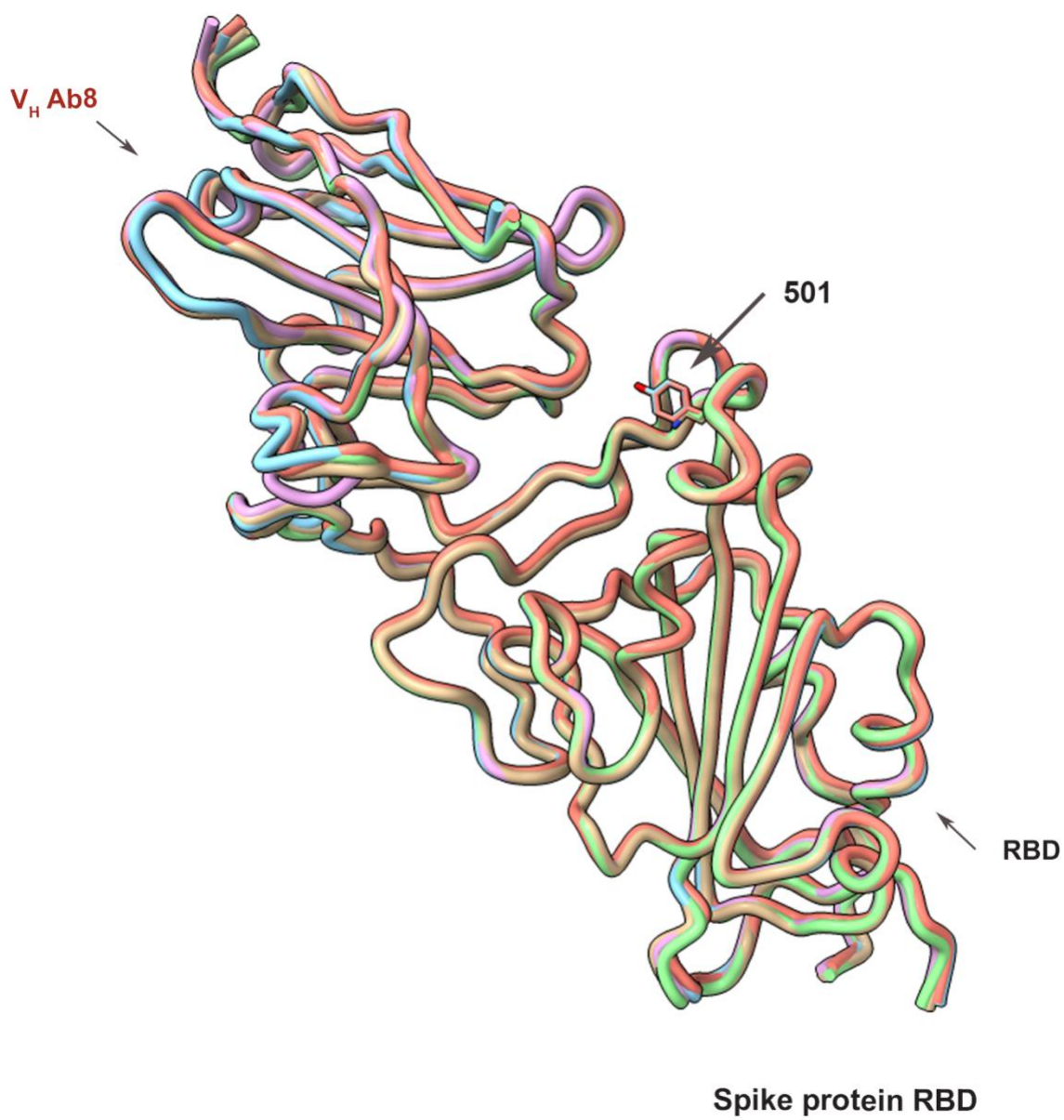


Figure S5